Materials Advances

ROYAL SOCIETY OF CHEMISTRY

PAPER

View Article Online
View Journal | View Issue

Cite this: *Mater. Adv.*, 2026, 7, 3221

Bi^{3+}-sensitized up-conversion luminescence and non-contact optical thermometry in $NaCaYV_2O_8:Er^{3+}/Yb^{3+}$ phosphors

Fadwa Ayachi,[a] Kamel Saidi,[ab] I. Mediavilla-Martínez,[c] Mohamed Dammak*[a] and J. Jimenez[c]

Tri-doped $NaCaYV_2O_8$ phosphors incorporating Er^{3+}, Yb^{3+}, and variable Bi^{3+} concentrations (0–0.15 mol%) were synthesized *via* a sol–gel route. Phase purity and particle morphology were verified through X-ray diffraction (XRD) and Transmission electron microscopy (TEM). Optical spectroscopy revealed that Bi^{3+} incorporation mediates defect-state-induced band gap contraction (from 3.2 to 3.05 eV), facilitating enhanced energy transfer coupling within the Er^{3+}/Yb^{3+} system. Under 980 nm excitation, pronounced green up conversion signals emerged at 525 and 552 nm, attributed to the $^2H_{11/2} \rightarrow {}^4I_{15/2}$ and $^4S_{3/2} \rightarrow {}^4I_{15/2}$ transitions of Er^{3+}. Photoluminescence intensity scaled monotonically with Bi^{3+} content up to an optimum at 0.07 mol, beyond which non-radiative losses dominated. Temperature-dependent up conversion spectroscopy (298–513 K) demonstrated that fluorescence intensity ratios (FIR) derived from the thermally coupled $^2H_{11/2}$ and $^4S_{3/2}$ manifolds enabled reliable ratiometric thermometry independent of excitation fluctuations. The 7 mol% Bi^{3+}-doped composition exhibited the highest absolute (S_a) and relative (S_r) thermal sensitivities, establishing this composition as optimal for simultaneous up conversion brightness and temperature-sensing performance. The findings underscore the strategic value of bismuth co-doping in vanadate hosts for synergistic enhancement of both luminescence efficiency and metrological precision.

Received 7th January 2026,
Accepted 14th February 2026

DOI: 10.1039/d6ma00035e

rsc.li/materials-advances

1. Introduction

Lanthanide-doped up conversion (UC) materials have garnered significant attention in recent years due to their versatility in frontier applications ranging from photothermal therapy and bioimaging to contactless temperature sensing.[1–4] The distinct optical signatures of these phosphors arise from the rich electronic structure of trivalent rare-earth (RE^{3+}) ions, which possess abundant metastable energy levels that facilitate efficient photon absorption and emission.[5,6] Among these applications, optical thermometry based on thermally coupled levels (TCLs) is scientifically paramount as it allows for precise thermal reading without physical contact. This mechanism is particularly effective in Er^{3+} ions, where the $^2H_{11/2}$ and $^4S_{3/2}$ excited states are separated by an energy gap of approximately 800 cm^{-1}, allowing for population redistribution governed by Boltzmann statistics and mediated by host lattice phonons.[7–14]

Despite the promise of these materials, enhancing their emission efficiency remains a critical challenge. One effective strategy involves modifying the local crystal field by introducing metal cations (*e.g.*, Li^+, Zn^{2+}, Mg^{2+}), which has been shown to modulate the host environment and improve UC performance.[15] More recently, the incorporation of Bismuth (Bi^{3+}) as a sensitizer has emerged as a powerful approach. Optimal Bi^{3+} doping can significantly amplify UC emission intensity of RE^{3+} systems through defect engineering and energy transfer modification.[16] While the benefits of Bi^{3+} are known in other hosts, the specific impact of Bi^{3+} co-doping on the optical and thermal properties of the $NaCaYV_2O_8:Er^{3+}/Yb^{3+}$ system remains unexplored. This investigation is vital because the Fluorescence Intensity Ratio (FIR) technique relies heavily on optimizing host-dopant interactions to achieve the high accuracy and resolution required for practical non-contact thermometry.[17,18] Consequently, maximizing the thermal sensitivity of Er^{3+}/Yb^{3+} codoped phosphors continues to be a priority in contactless thermometry research.[19,20]

In this work, we report the synthesis of $NaCaYV_2O_8$ (NCYVO) phosphors co-doped with Er^{3+}/Yb^{3+}, with varying concentrations of Bi^{3+} *via* a sol–gel method. Structural and morphological properties were characterized using X-ray diffraction (XRD), while the role of Bi^{3+} in modulating the UC emission intensity

[a] *Laboratoire de Physique Appliquée, Faculté des Sciences de Sfax, Département de Physique, Université de Sfax, BP 1171, Sfax, Tunisia. E-mail: madidammak@yahoo.fr, Mohamed.dammak@fss.usf.tn*
[b] *Department of Physics, Sfax Preparatory Engineering Institute, University of Sfax, 1172- 3000, Sfax, Tunisia*
[c] *GdS Optronlab, Department of Condensed Matter Physics, LUCIA Building University of Valladolid, Paseo de Belen 19, 47011, Valladolid, Spain*

was systematically investigated. Furthermore, detailed temperature-dependent luminescence measurements were conducted to evaluate the UC mechanism and determine the suitability of these phosphors for high-sensitivity optical thermometry applications.

2. Experimental section

2.1. Synthesis

A series of Bi^{3+} co-doped NCYVO:0.02Er^{3+}/0.10Yb^{3+} phosphors with Bi^{3+} concentrations (x = 0, 5, 7, 10 and 15) were prepared *via* a citrate-assisted sol–gel route. High-purity reagents were used as received from Sigma-Aldrich without further purification. The precursor materials comprised calcium nitrate [$Ca(NO_3)_2$, 99.9%], ammonium metavanadate [NH_4VO_3, 99.96%], and the rare-earth/metal nitrates: $Y(NO_3)_3{\cdot}6H_2O$ (99.9%), $Yb(NO_3)_3{\cdot}5H_2O$ (99.9%), $Er(NO_3)_3{\cdot}5H_2O$ (99.9%), and $Bi(NO_3)_3{\cdot}5H_2O$ (99.9%). Citric acid [$C_6H_8O_7$, 99.0%] served as the chelating agent. In a typical synthesis, stoichiometric amounts of the metal precursors were dissolved in 120 mL of deionized water in a 250 mL beaker. The mixture was stirred continuously at ambient temperature until a transparent, homogeneous solution was achieved. Citric acid was then added in a 1 : 1 molar ratio to the total metal ions, and the pH was adjusted to ~7 using ammonium hydroxide under vigorous stirring to form the citrate-metal complexes. The solution was evaporated at 80 °C on a hotplate with continuous stirring until a viscous gel formed, followed by drying in an oven at 120 °C for 12 h to obtain a dry xerogel. The xerogel was ground into a fine powder and pre-calcined at 500 °C for 4 h in air to decompose organic residues. Finally, the powder was pelletized, annealed at 900 °C for 6 h in air using a muffle furnace with a heating rate of 5 °C min^{-1}, and slowly cooled to room temperature to yield the crystalline phosphor samples.

2.2. Characterization

The crystal structure and phase purity of the synthesized phosphors were characterized by powder X-ray diffraction (XRD) using a Rigaku D-Max 2500 diffractometer equipped with graphite-monochromatized Cu Kα radiation (λ = 1.5406 Å). Diffraction patterns were collected over a 2θ range of 10°–80° at a scanning speed of 15° min^{-1}. Photoluminescence (PL) spectra were recorded using a PerkinElmer spectrophotometer to evaluate the up-conversion emission properties of the phosphors.

3. Results and discussions

3.1. XRD

The phase purity and structural evolution of NaCaY-V_2O_8:0.02Er^{3+}/0.10Yb^{3+}/$x$$Bi^{3+}$ phosphors (x = 0, 0.05, 0.07, 0.10, 0.15 mol%) were examined using X-ray diffraction, as shown in Fig. 1(a). All diffraction patterns exhibit well-defined peaks that can be fully indexed to the standard monoclinic $NaCaYV_2O_8$ phase (JCPDS No. 96-152-7822), confirming the formation of a single-phase material across the entire Bi^{3+} doping range. No additional diffraction peaks corresponding to secondary phases or impurity compounds are detected, indicating that Bi^{3+} ions are successfully incorporated into the $NaCaYV_2O_8$ host lattice without altering its crystal structure. The mean crystallite size (D_{W-H}) and lattice strain (ε) of all samples were determined from the Bragg peak positions and their full width at half maximum (β) by applying the Williamson–Hall method.[21]

$$\beta\cos\theta = \frac{k\lambda}{D_{W-H}} + 4\varepsilon\sin\theta$$

here, θ represents the diffraction angle corresponding to the most intense peak, K is the shape factor taken as 0.9, and λ denotes the wavelength of the Cu Kα radiation (λ = 0.154 nm). The variation observed in the Williamson–Hall plots presented

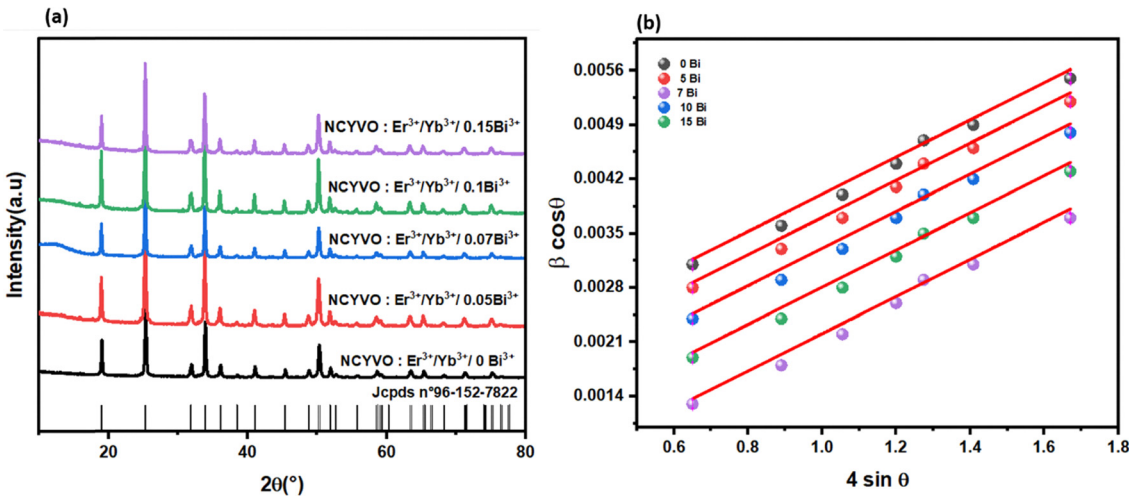

Fig. 1 (a) X-ray diffraction (XRD) patterns of the synthesized $NaCaYV_2O_8$:0.02Er^{3+}/0.10Yb^{3+} phosphors doped with varying concentrations of Bi^{3+} (x = 0, 0.05,0.07, 0.10, 0.15 mol%) and (b)Williamson–Hall plots of $NaCaYV_2O_8$:0.02Er^{3+}/0.10Yb^{3+} phosphors doped with varying concentrations of Bi^{3+} (x = 0, 0.05,0.07, 0.10, 0.15 mol%).

in Fig. 1(b) allows the determination of the crystallite size (D_{W-H}) and lattice strain (ε) for the synthesized samples, as summarized in Table S1. Based on the Williamson–Hall analysis, the 0.07 mol% Bi^{3+}-doped phosphor exhibits the lowest lattice strain, indicating superior structural quality compared to the other compositions.

Rietveld refinement was performed on the representative diffraction profiles in order to quantify the structural parameters (Fig. S1). The refined crystallographic data, including lattice constants and reliability factors, are compiled in Table S1. The low residual values (R_{wp}, and R^2) accounts for the high quality of the fit and the purity of the as-synthesized samples. The unit cell volume exhibits a consistent increase with rising Bi^{3+} content, as shown in Table S1, which serves as direct confirmation of the substitution of Y^{3+} by the larger Bi^{3+} ion. This expansion aligns with Vegard's law, thereby supporting the notion of Bi^{3+} occupancy at the Y^{3+} site; the ionic radius of Bi^{3+} (117 pm, CN = 8) is approximately 15% larger than that of Y^{3+} (101.9 pm, CN = 8). While Na^{+} (118 pm) and Ca^{2+} (112 pm) possess similar radii, substitution at these sites would necessitate charge compensation due to the trivalent character of Bi^{3+}, a process that is energetically unfavorable in the absence of co-dopants or vacancies. Conversely, the isovalent substitution of Y^{3+} with Bi^{3+} circumvents these issues, thereby designating the Y-site as the most likely location for incorporation. This observation supports the effective integration of Bi^{3+} within the cationic sublattice of the $NaCaYV_2O_8$ host material.

3.2. TEM analysis

The microstructural evolution of the NCYVO:$0.02Er^{3+}/0.10Yb^{3+}/x Bi^{3+}$ phosphors (x = 0 and 0.07 mol) was examined by Transmission electron microscopy TEM, as shown in Fig. 2(a and b) and TEM micrographs of Bi^{3+}-doped samples with higher dopant concentrations: (a) 0.05 Bi^{3+}, (b) 0.1 Bi^{3+}, and (c) 0.15 Bi^{3+} are provided in the Fig. S2.

All samples exhibit increased particle agglomeration and irregular morphologies compared to the undoped material, consistent with the trend observed for the 7% Bi^{3+}-doped sample in the main text. The scale bar in all images is 200 nm. Fig. 2(a) shows well-defined, faceted nanoparticles corresponding to the undoped sample (0 Bi^{3+}), where the particles are relatively uniform in size and loosely aggregated, indicating good dispersion and stable crystal growth. In contrast, Fig. 2(b) represents the sample doped with 0.07 Bi^{3+}, which exhibits a more compact and irregular morphology with pronounced agglomeration and less distinguishable particle boundaries. The increased aggregation and morphological distortion observed in the Bi^{3+}-doped sample suggest that higher Bi^{3+} incorporation affects the crystal growth process, likely by introducing lattice distortion and enhanced interparticle interactions. Overall, Bi^{3+} doping at 0.07 leads to reduced particle uniformity and increased agglomeration compared to the undoped material.

3.3. Optical studies

3.3.1. Band gap value calculations. The ultraviolet–visible (UV-vis) absorption spectrum of NCYVO was obtained using diffuse reflectance measurements and analyzed through the Kubelka–Munk function to elucidate the compound's semiconductor characteristics.[22,23]

$$F(R) = \frac{(1-R)^2}{2R} \quad (1)$$

R represents the reflectance.

The optical band gap (E_g) of the compound was determined using the Tauc relation.

$$(F(R) \times h\vartheta)^n = B(h\vartheta - E_g) \quad (2)$$

where the absorption coefficient (α) is related to a proportionality constant (B), and E_g represents the optical band gap energy. The exponent n can take values of 0.5, 1.5, 2, or 3, corresponding to different types of optical transitions (direct allowed, direct forbidden, indirect allowed, and indirect forbidden, respectively).

The diffuse reflectance spectra (DRS) of the Bi^{3+} co-doped NCYVO:Er^{3+}/Yb^{3+} phosphors were recorded in the 200–1100 nm range, as presented in Fig. 3. The spectra are dominated by a strong ultraviolet absorption band between 200–350 nm, corresponding to the O^{2-} to V^{5+} charge transfer (CT) transition within the VO_4^{3-} tetrahedral groups. Superimposed on this host absorption are sharp, discrete peaks in the visible and

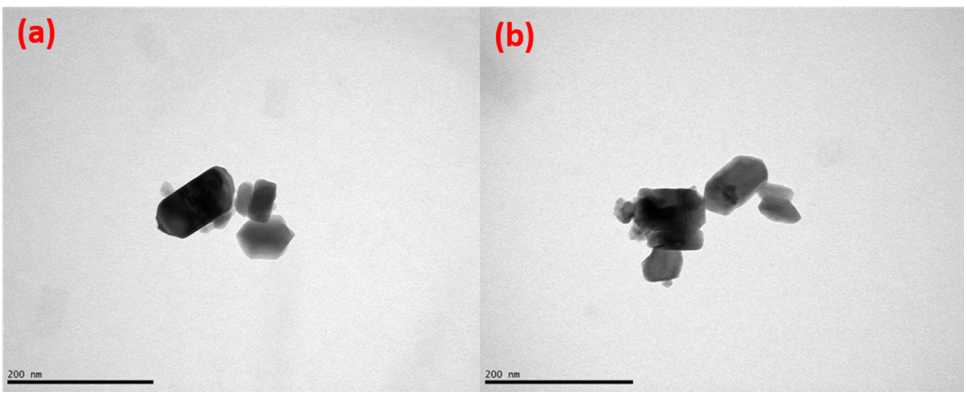

Fig. 2 Transmission electron microscopy (TEM) images illustrating the surface morphology of $NaCaYV_2O_8$:$0.02Er^{3+}/0.10Yb^{3+}$ phosphors with different Bi^{3+}concentrations: (a) 0 mol, (b) 0.07 mol%.

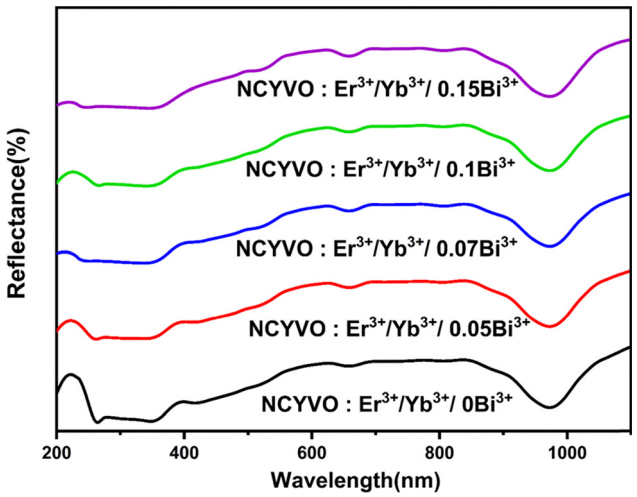

Fig. 3 UV-vis diffuse reflectance spectra (DRS) of the NCYVO:0.02Er^{3+}/0.10Yb^{3+} phosphors co-doped with varying concentrations of Bi^{3+} (x = 0–0.15 mol).

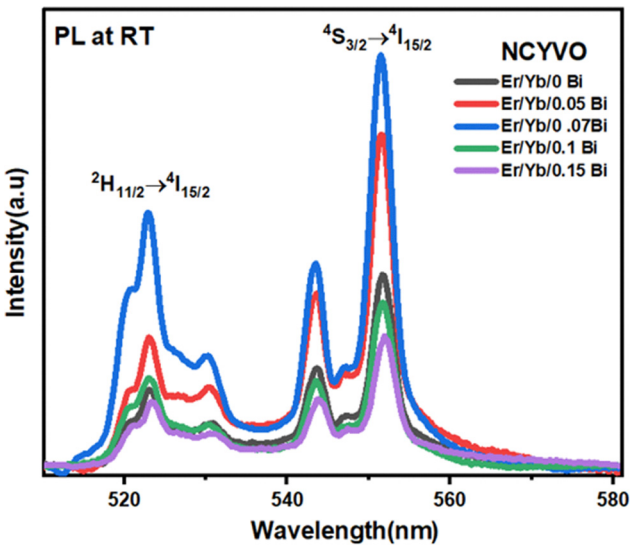

Fig. 4 Up conversion (UC) emission spectra of the NCYVO:0.02Er^{3+}/0.10 Yb^{3+} phosphors doped with various Bi^{3+} concentrations (x = 0–0.15 mol) under 980 nm excitation.

near infrared regions, which are assigned to the characteristic 4f–4f intra-configurational transitions of Er^{3+} ions.[24] Notably, the broad absorption centered at 980 nm arises from the $^2F_{7/2}$ to $^2F_{5/2}$ transition of Yb^{3+}, which is critical for efficient photon harvesting and subsequent energy transfer to Er^{3+} activators.[25,26] Upon Bi^{3+} doping, a new absorption feature emerges at 353 nm, attributed to the 1S0 to 3P1 transition of Bi^{3+} ions, confirming their successful incorporation into the lattice.[27] Furthermore, the absorption edge exhibits a progressive redshift with increasing Bi^{3+} concentration. As shown in Fig. S3, the optical band gap (E_g) narrows monotonically from 3.2 eV for the Bi-free sample to 3.05 eV for the 0.15 mol Bi^{3+} sample. This band gap contraction is ascribed to the hybridization of the Bi^{3+} $6s^2$ orbitals with the O–2p valence bands, which elevates the valence band maximum and introduces localized defect states within the forbidden gap.[16,28] These intermediate states effectively broaden the absorption cross-section and may serve as bridges for energy transfer, thereby modulating the optical performance of the phosphor.[21,22]

3.3.2. Luminescence properties. The influence of Bi^{3+} sensitization on the up conversion (UC) performance was evaluated by recording the emission spectra of NCYVO:0.02Er^{3+}/0.10Yb^{3+}/$x$$Bi^{3+}$ phosphors under 980 nm diode laser excitation (Fig. 4). All the samples display the characteristic green emission bands centered at 525 nm and 552 nm. These bands are assigned to thermally coupled $^2H_{11/2} \rightarrow {}^4I_{15/2}$ and $^4S_{3/2} \rightarrow {}^4I_{15/2}$ transitions of Er^{3+} respectively.[29] It should be noted that no emissions directly attributable to Bi^{3+} were detected in the visible range, confirming its role as sensitizer or host modifier rather than a direct activator in this spectral window.

As illustrated in Fig. 4, the UC emission intensity exhibits a strong dependence on Bi^{3+} concentration. The integrated green luminescence intensity enhances monotonically with increasing Bi^{3+} content, reaching a maximum at 7 mol%. This enhancement is attributed to the Bi^{3+}-induced modification of the local crystal field symmetry around the Er^{3+}/Yb^{3+} ions, which relaxes the selection rules for 4f–4f transitions, and the defect-mediated energy transfer pathways established by the narrowed band gap. However, for doping levels exceeding 0.07 mol a systematic decline in intensity is observed.

The emission spectra for each sample at different pump powers are studied without saturation at high powers. The emission intensity *vs.* the pump power will follow the relation:

$$I \propto (P)^n \quad (3)$$

where I, P, and n stand for the up-conversion intensity, pump power, and the exponent, that represents the number of photons absorbed per emitted photon, respectively.[30–32] To elucidate the photon absorption mechanism governing the up-conversion process, the dependence of emission intensity I on pump power P was investigated for all Bi^{3+}-doped samples. According to the relation $I \propto (P)^n$ the slope of the linear fit in a log–log plot (Fig. S3(a–e)) provides the n value. For all phosphor compositions, the calculated slopes lie in the range of 1.57–1.97. These values are close to the theoretical limit of n = 2 confirming that a two-photon absorption process is the dominant mechanism responsible for the observed green up conversion emission.

Based on these results and the simplified energy level diagram (Fig. S3(f)), the proposed UC mechanism involves a synergistic interplay of Ground State Absorption (GSA), Energy Transfer Up conversion (ETU), and Cooperative Energy Transfer (CET). Upon 980 nm excitation, Yb^{3+} ions (sensitizers) efficiently absorb incident photons *via* the $^2F_{7/2} \rightarrow {}^2F_{5/2}$ transition due to their large absorption cross-section. Subsequently, excited Yb^{3+} transfers energy to a proximal Er^{3+} ion, promoting it from the ground state $^4I_{15/2}$ to the intermediate $^4I_{11/2}$ level. A second energy transfer event from another excited Yb^{3+} ion (or the absorption of a second photon by an already excited Er^{3+} ion *via* GSA/ESA) further excites the Er^{3+} population to the higher-lying $^4F_{7/2}$ manifold. Additionally, Cooperative Energy

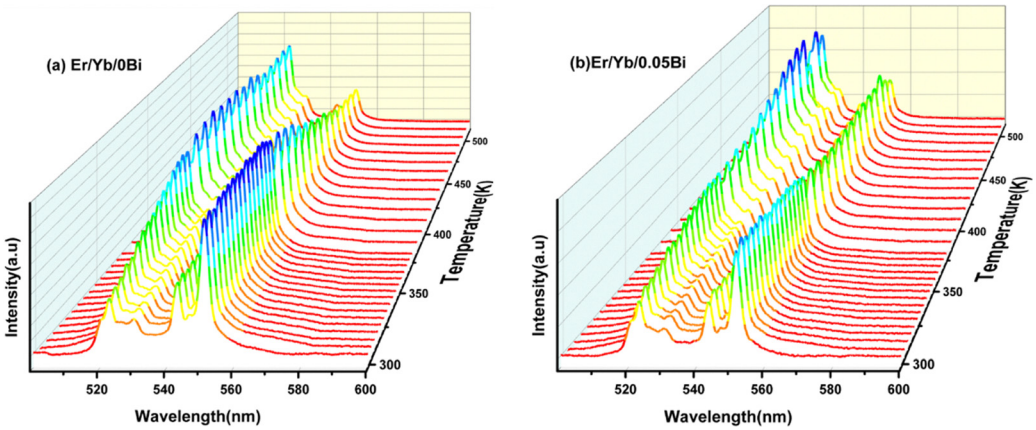

Fig. 5 Temperature-dependent up conversion (UC) emission spectra of (a) NCYVO:Er^{3+}/Yb^{3+}/0Bi^{3+} and (b) NCYVO:Er^{3+}/Yb^{3+}/0.05 Bi^{3+} under 980 nm excitation.

Transfer (CET) may occur, where two excited Yb^{3+} ions simultaneously transfer energy to a single Er^{3+} ion, directly bridging the gap to the $^4F_{7/2}$ state. Following rapid non-radiative relaxation to the metastable $^2H_{11/2}$ and $^4S_{3/2}$ levels, the ions decay radiatively to the ground state, generating the characteristic green emissions at 525 nm and 552 nm, respectively.[30]

3.3.3. Temperature sensing behavior. To evaluate the suitability of the Bi^{3+}-sensitized NCYVO:Er^{3+}/Yb^{3+} phosphors for non-contact thermometry, temperature-dependent up conversion spectra were recorded in the range of 298–513 K, under 980 nm excitation, as shown in Fig. 5(a and b) NCYVO:Er^{3+}/Yb^{3+} doped 0 and 0.07 respectively and Fig. S4(a–c) for Er/Yb/XBi (X = 0.05,0.1,0.15). The thermometric performance relies on the thermally coupled levels (TCLs) of the Er^{3+} ion: the $^2H_{11/2}$ state (emitting at 525 nm) and the $^4S_{3/2}$ state (emitting at 552 nm). Given the relatively small energy gap (ΔE < 2000 cm^{-1}) between these manifolds, the population redistribution is governed by quasi-thermal equilibrium. As the temperature rises, electrons are promoted from the lower $^4S_{3/2}$ level to the higher $^2H_{11/2}$ level, resulting in a characteristic increase in the 525 nm emission intensity relative to the 552 nm emission.

This redistribution follows Boltzmann statistics, allowing the fluorescence intensity ratio (FIR) to be defined as a function of absolute temperature T according to eqn (4):[33,34]

$$\mathrm{FIR} = \frac{I_H}{I_S} = B \times \mathrm{Exp}\left(\frac{-\Delta E}{K_B T}\right) \quad (4)$$

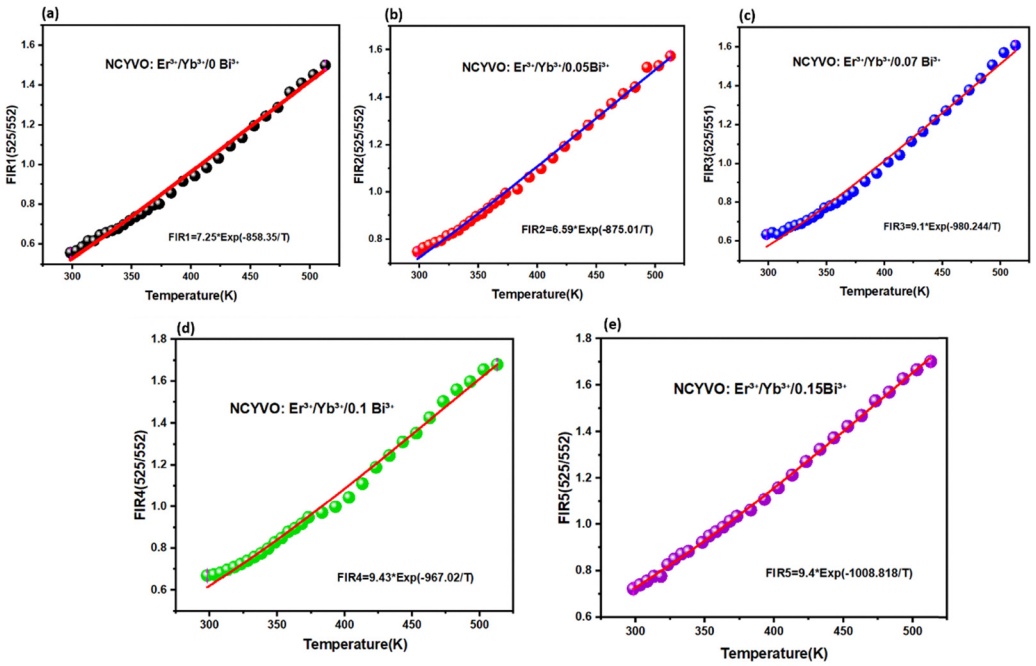

Fig. 6 The variation of FIR with temperature for (a) NCYVO:Er^{3+}/Yb^{3+}/0 Bi^{3+}, (b) NCYVO:Er^{3+}/Yb^{3+}/0.05 Bi^{3+}, (c) NCYVO:Er^{3+}/Yb^{3+}/0.7 Bi^{3+}, (d) NCYVO:Er^{3+}/Yb^{3+}/0.1Bi^{3+}, and (e) NCYVO:Er^{3+}/Yb^{3+}/0.15Bi^{3+}.

Table 1 $\Delta E/K_B$, S_r, S_a, δFIR/FIR values of NCYVO:$Er^{3+}/Yb^{3+}/xBi^{3+}$ (x = 0,0.05,0.07,0.10 and 0.15)

Bi^{3+} concentration	$\Delta E/K_B$ (K)	$S_{a\,max}$	S_r (300 K)	σ = δFIR/FIR
0	858.35	0.00540 (430 K)	0.75%	0.0012
0.05	875.01	0.004 (440 K)	0.48%	0.0013
0.07	980.244	0.005 (480 K)	0.65%	0.0034
0.1	987.02	0.00515 (470 K)	0.63%	0.0551
0.15	1008.818	0.005 (513 K)	0.5%	0.0065

where I_H and I_S represent the integrated intensities of the $^2H_{11/2} \rightarrow {}^4I_{15/2}$ (525 nm) and $^4S_{3/2} \rightarrow {}^4I_{15/2}$ (552 nm) emission bands, respectively. The pre-exponential factor B is a constant determined by the spontaneous emission rates, degeneracies, and angular frequencies of the transitions, K_B is the Boltzmann constant, and ΔE is the effective energy gap. A crucial advantage of this ratiometric method is that the FIR value is independent of fluctuations of the excitation power, or losses in the optical path, ensuring high measurement precision and stability for practical sensing applications.

Fig. 6(a–e) show that the fluorescence intensity ratios (FIR) between the thermally coupled $^2H_{11/2}$ and $^4S_{3/2}$ levels increase non-linearly for the $Er^{3+}/Yb^{3+}/xBi^{3+}$ tri-doped NCYVO phosphor samples (x = 0, 0.05, 0.07, 0.10, and 0.15) from 298 to 513 K. The ($\Delta E/K_B$) values obtained from the fitting results for all samples are summarized in Table 1. The temperature sensitivity of the phosphor samples is a critical factor in the development of highly responsive optical temperature sensors. Among the key indicators used to evaluate and compare sensor performance are the absolute sensitivity (S_a) and relative sensitivity (S_r). These parameters offer meaningful insights into the sensing efficiency of the material and can be calculated using the following equations eqn (5) and (6), respectively.[35–37]

$$S_a = \frac{dFIR}{dT} \quad (5)$$

$$S_r = \frac{1}{FIR} \cdot \frac{dFIR}{dT} \quad (6)$$

Fig. 7(a–e) present the temperature-dependent evolution of the absolute sensitivity S_a for the different Bi^{3+} concentrations in NCYVO:$Er^{3+}/Yb^{3+}/xBi^{3+}$. The values of S_a were obtained from the FIR–temperature relationship using eqn (5). S_a increases steadily with temperature and reaches a maximum at a characteristic temperature T_{max} specific to each composition. These maximum values are listed in Table 2. A clear decline in the peak S_a is observed as the Bi^{3+} concentration increases, indicating that the sample without Bi^{3+} (x = 0) exhibits the highest absolute sensitivity, approximately 5.4 × 10^{-3} K^{-1} at 430 K.

This behavior indicates that the variation of S_a is primarily governed by the pre-exponential factor B in the FIR expression, whereas the energy gap ΔE between the thermally coupled levels mainly determines the optimal operating temperature range. Within the Judd–Ofelt formalism, the parameter B can be expressed in terms of the intensity parameters Ω_λ (λ = 2,4,6), which reflect the local crystal-field symmetry and the degree of covalency surrounding the Er^{3+} ions. In practice, these Ω_λ values and thus B can be derived from room-temperature absorption or emission spectra, or extracted from literature for Er^{3+} in structurally similar hosts, providing a predictive framework for estimating S_a without time consuming temperature-dependent measurements.

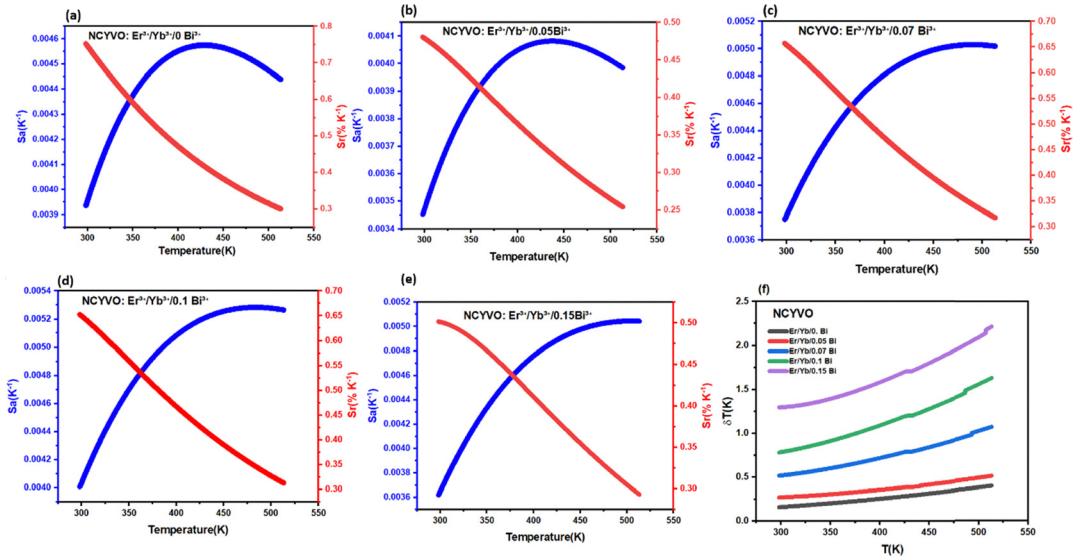

Fig. 7 The variations of absolute sensitivity (S_a) and relative sensitivity (S_r) with temperature for (a) NCYVO:Er^{3+}/Yb^{3+}/0%Bi^{3+}, (b) NCYVO:Er^{3+}/Yb^{3+}/5%Bi^{3+}, (c) NCYVO:Er^{3+}/Yb^{3+}/7% Bi^{3+}, (d) NCYVO:Er^{3+}/Yb^{3+}/10%Bi^{3+}, and (e) NCYVO:Er^{3+}/Yb^{3+}/15% Bi^{3+} under 980 nm excitation, (f) the variations of temperature resolution (δT) with temperature for NCYVO:Er^{3+}/Yb^{3+}/X Bi^{3+} (X = 0,0.05,0.07,0.1 and 0.15) under 980 nm excitation.

Table 2 Temperature sensitivity comparison of phosphors

Sensing materials	Temperature range (K)	Excitation (nm)	$S_{a\,max}$ (K^{-1})	S_r (%K^{-1})	Ref.
$NaErF_4$@$NaYF_4$@$NaYbF_4$:Tm@$NaYF_4$ NPs	293–413	980	—	0.71 (315 K)	43
$GdPVO_4$:2%Er^{3+}/15%Yb^{3+}	300–440	980	0.00507 (320 K)	0.63 (300 K)	44
$LaNbO_4$:1%Er^{3+}/10%Yb^{3+}	10–300	980	—	0.749 (300 K)	45
$CaLa_2ZnO_5$:Er^{3+}/Yb^{3+}	298–513	980	—	0.59 (513 K)	46
Tellurite glass:Yb^{3+}, Er^{3+}	298–473	980	—	0.53 (298 K)	47
$K_3Y(PO_4)_2$:Yb^{3+}/Ho^{3+}	303–523	980	—	0.2 (303 K)	48
$NaCaYV_2O_8$:Er^{3+}/Yb^{3+}/0.07Bi^{3+}	298–513	980	0.0051 (430 K)	0.65 (300 K)	This work

For the FIR involving the transitions $^2H_{11/2} \rightarrow {}^4I_{15/2}$ and $^4S_{3/2} \rightarrow {}^4I_{15/2}$, B is approximated using eqn (7), which relates it to Ω_2, Ω_4, Ω_6, and the corresponding reduced matrix elements. Among these parameters, Ω_2 is particularly sensitive to local structural modifications and bonding characteristics, while Ω_4 and Ω_6 remain comparatively stable and are primarily dictated by the host lattice. Therefore, in the NCYVO system, Ω_2 appears to be the dominant Judd–Ofelt parameter influencing the evolution of B, and consequently the absolute sensitivity S_a.[38]

$$B = \frac{3.35\Omega_2 + 1.94\Omega_4 + \Omega_6}{\Omega_6} \quad (7)$$

The variation of relative sensitivity (S_r), a critical figure of merit for comparing sensors across different temperature ranges, was calculated using eqn (6) and is presented in Fig. 7. Unlike absolute sensitivity, S_r typically follows a $1/T^2$ dependence. The maximum S_r values, obtained at 300 K, are listed in Table 1. Remarkably, while Bi^{3+} doping modulates the absolute sensitivity, the relative sensitivity remains robust, ensuring high precision for physiological temperature sensing.

To benchmark the performance of the NCYVO:Er^{3+}/Yb^{3+}/xBi^{3+} system, the obtained S_a and S_r values were compared with those of other Er^{3+}-based optical thermometers reported in the literature (Table 2). The sensitivity values achieved in this work even for the Bi-doped samples exceed those of many established hosts (*e.g.*, fluorides, oxides, and other vanadates). This superior performance, combined with the significant enhancement in emission intensity provided by Bi^{3+} sensitization, positions the 0.07 Bi^{3+}-doped NCYVO phosphor as a highly promising candidate for practical, high-sensitivity optical thermometry applications.

Thermal resolution (δT) is another parameter used to evaluate the performance of the proposed high-temperature sensor. It quantifies the minimum temperature difference that the sensor can reliably detect, thus reflecting its ability to discern small changes in temperature with precision. A lower δT value indicates a higher sensitivity of the sensor to temperature variations. This parameter was calculated using the following equation, as presented in eqn (8).[39,40]

$$\delta T = \frac{1}{S_r} \cdot \frac{\delta FIR}{FIR} \quad (8)$$

The parameter δFIR defines the experimental uncertainty of the thermometric signal, effectively setting the threshold for the smallest detectable change in the fluorescence ratio. While this limit is intrinsic to the sensor's performance, it is also

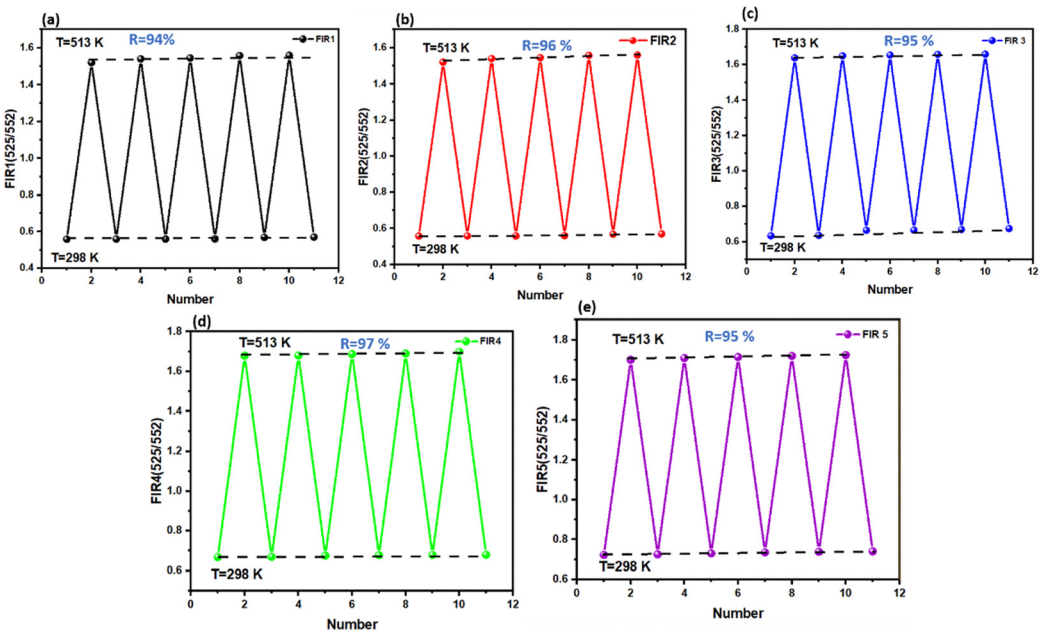

Fig. 8 Repeatability assessment (R) (a) Er/Yb/0 Bi (b) Er/Yb/0.05 Bi, (c) Er/Yb/0.07Bi, (d) Er/Yb/0.1 Bi and (e) Er/Yb/0.15 Bi for NCYVO phosphors.

heavily dependent on the instrumentation and environmental conditions. To minimize this uncertainty and enhance the resolution, we optimized the data acquisition protocol by increasing the signal integration time and averaging consecutive spectral scans to suppress random experimental noise.

To quantify the detection limit, a statistical analysis was performed using 50 consecutive measurements taken at room temperature for the NCYVO:Er/Yb/x%Bi samples (x = 0, 5, 7, 10, 15). The distribution of these measurements is visualized in the histograms in Fig. S4(a–e). The relative uncertainty of the signal, defined as δFIR/FIR, was derived from the standard deviation of these distributions. The calculated values for all doping concentrations are cataloged in Table 2. This metric serves as a direct indicator of measurement precision and system stability.

Furthermore, Fig. 7(f) illustrates the evolution of the thermal resolution δT as a function of temperature for the NCYVO:Er/Yb/xBi samples (x = 0, 0.05, 0.07, 0.10, 0.15). The calculated max values δT_{max} for all the doping concentrations are listed in Table 2. The data indicate that the thermal resolution improved with doping, yielding smaller δT as the temperature increased. This trend underscores the sensor's enhanced capability to discriminate minute temperature fluctuations in the higher temperature regimes across the investigated samples.

The estimated thermometric parameters (FIR values) were carefully measured during multiple cycles of the sample between ambient temperature (298 K) and increased temperatures (513 K), as shown in Fig. 8, in order to verify the accuracy of the used temperature sensing methods. The following formula was used to determine the repeatability(R):[41,42]

$$R_p(100\%) = 1 - \frac{\max M_i(T)_c \times M(T)_c}{\mathrm{FIR}_c} \times 100$$

where $M(T)_c$ across 10 cycles and $M_i(T)_c$ for the measured parameter (FIR) in the ith cycle are represented. The calculated FIR values show reversible temperature changes; within the measured temperature range, the FIR values for Er/Yb/xBi (x = 0,0.05,0.07,0.1 and0.15) are 94%, 96%, 95%, 97% and 95% respectively. This demonstrates how are highly reliable and repeatable the thermometric techniques used.

4. Conclusions

In summary, Bi^{3+}-sensitized $NaCaYV_2O_8$:Er^{3+}/Yb^{3+} up conversion phosphors were successfully synthesized *via* a sol–gel method, their structural, optical, and thermometric properties were systematically investigated. Structural analysis confirmed the formation of a single-phase solid solution, where Bi^{3+} incorporation induces a controlled reduction in the optical band gap (from 3.2 to 3.05 eV) *via* spin–orbit hybridization. This electronic structure modulation, combined with local symmetry distortion, facilitates efficient energy transfer and relaxes the selection rules for 4f–4f transitions, leading to a significant enhancement in the green up conversion emission intensity.

The optimal doping concentration was identified as 0.07 mol Bi^{3+}, which balances the emission brightness with concentration quenching effects. Temperature-dependent luminescence studies (298–513 K) demonstrated that the fluorescence intensity ratio (FIR) of the thermally coupled Er^{3+} levels $^2H_{11/2} \rightarrow {}^4S_{3/2}$ enables reliable non-contact thermometry. Although Bi^{3+} doping resulted in a trade-off with absolute sensitivity (S_a), the optimized phosphor retained high relative sensitivity (S_r) and excellent thermal resolution δT, superior to many existing vanadate-based sensors. These results establish the 0.02Er^{3+}/0.10Yb^{3+}/0.07Bi^{3+} tri-doped NCYVO phosphor as a robust, multifunctional material suitable for advanced applications in optical thermometry, photonic sensing, and optoelectronics.

Conflicts of interest

There are no conflicts to declare.

Data availability

All data underlying the results are available as part of the article and no additional source data are required.

Supplementary information (SI) is available. See DOI: https://doi.org/10.1039/d6ma00035e.

References

1 Z. Zhang, D. Zhu, Z. Huang, Z. Zhu, J. Liu and K. Li, Thermally boosted color-tunable up-conversion luminescence in $Gd_{2-x}La_xZr_3(MoO_4)_9$: Yb^{3+}, Ln^{3+} (Ln = Er, Ho, Tm) for advanced anti-counterfeiting and wide-range-high-sensitivity optical thermometry applications, *Mater. Today Chem.*, 2025, **48**, 102971, DOI: 10.1016/j.mtchem.2025.102971.
2 J. Liu, W. Bu, S. Zhang, F. Chen, H. Xing, L. Pan, L. Zhou, W. Peng and J. Shi, Controlled Synthesis of Uniform and Monodisperse Upconversion Core/Mesoporous Silica Shell Nanocomposites for Bimodal Imaging, *Chem. – Eur. J.*, 2012, **18**, 2335–2341, DOI: 10.1002/chem.201102599.
3 C. Zheng, C. P. Teng, D.-P. Yang, M. Lin, K. Y. Win, Z. Li and E. Ye, Fabrication of luminescent TiO_2:Eu^{3+} and ZrO_2:Tb^{3+} encapsulated PLGA microparticles for bioimaging application with enhanced biocompatibility, *Mater. Sci. Eng. C*, 2018, **92**, 1117–1123, DOI: 10.1016/j.msec.2017.10.005.
4 L.-D. Sun, Y.-F. Wang and C.-H. Yan, Paradigms and Challenges for Bioapplication of Rare Earth Upconversion Luminescent Nanoparticles: Small Size and Tunable Emission/Excitation Spectra, *Acc. Chem. Res.*, 2014, **47**, 1001–1009, DOI: 10.1021/ar400218t.
5 Q. Li, Z. Zhang and K. Li, Tailoring up-conversion luminescence and enhancing temperature sensitivity through Tm^{3+} co-doping in Yb^{3+}, Er^{3+}/Ho^{3+} activated Ca(Gd,La)SbWO8 phosphors, *Ceram. Int.*, 2025, DOI: 10.1016/j.ceramint.2025.12.503.
6 A. Ćirić and S. Stojadinović, Structural and photoluminescence properties of Y_2O_3 and Y_2O_3: Ln^{3+} (Ln= Eu, Er, Ho)

films synthesized by plasma electrolytic oxidation of yttrium substrate, *J. Lumin.*, 2020, **217**, 116762.
7 S. Thakur, N. Dhiman, A. Sharma and A. K. Gathania, Effect of Photonic Structure on Optical Propertiesof YVO4:Eu^{3+} Phosphor, *J. Electron. Mater.*, 2017, **46**, 2085–2089, DOI: 10.1007/s11664-016-5133-x.
8 S. Kumar, R. Kumar and A. K. Gathania, Efficient and thermally stable Sm^{3+} -activated $Na_2BaCa(PO_4)_2$ phosphors for solid-state lighting and optical thermometry, *Mater. Res. Bull.*, 2026, **197**, 113939, DOI: 10.1016/j.materresbull.2025.113939.
9 P. Du, L. Luo and J. S. Yu, Tunable color upconverison emissions in erbium(III)-doped BiOCl microplates for simultaneous thermometry and optical heating, *Microchim. Acta*, 2017, **184**, 2661–2669, DOI: 10.1007/s00604-017-2278-0.
10 P. Du, L. Luo, H.-K. Park and J. S. Yu, Citric-assisted sol-gel based Er^{3+}/Yb^{3+} -codoped $Na_{0.5}Gd_{0.5}MoO_4$: A novel highly-efficient infrared-to-visible upconversion material for optical temperature sensors and optical heaters, *Chem. Eng. J.*, 2016, **306**, 840–848, DOI: 10.1016/j.cej.2016.08.007.
11 R. Dey and V. K. Rai, Yb^{3+} sensitized Er^{3+} doped La_2O_3 phosphor in temperature sensors and display devices, *Dalton Trans.*, 2014, **43**, 111–118.
12 M. Mondal, V. K. Rai and C. Srivastava, Influence of silica surface coating on optical properties of Er^{3+} -Yb^{3+}:$YMoO_4$ upconverting nanoparticles, *Chem. Eng. J.*, 2017, **327**, 838–848, DOI: 10.1016/j.cej.2017.06.166.
13 I. Kumar, Yashwinder, A. Kumar, S. Kumar, H. Thakur and A. K. Gathania, Charge compensation-driven downconverted luminescence enhancement in Er^{3+} -doped $SrTiO_3$ phosphors by co-doping with alkali ions (M + = Li, Na, K) for solid-state lighting applications, *Indian J. Phys.*, 2025, **99**, 2033–2042, DOI: 10.1007/s12648-024-03432-9.
14 A. Sharma, V. Sharma and A. K. Gathania, Enhancing photoluminescence properties of reddish-orange emitting phosphor cerium fluoride doped with Eu^{3+} by the incorporation of N-CQDs, *J. Alloys Compd.*, 2025, **1039**, 183032, DOI: 10.1016/j.jallcom.2025.183032.
15 D. Li, W. Qin, T. Aidilibike, P. Zhang, S. Liu, L. Wang and S. Li, Enhanced upconversion emission and magnetization in Yb^{3+} -Er^{3+}/Ho^{3+} codoped Gd2O3 nanocrystals by introducing Zn^{2+} ions, *J. Alloys Compd.*, 2016, **675**, 31–36, DOI: 10.1016/j.jallcom.2016.03.110.
16 R. S. Yadav, S. J. Dhoble and S. B. Rai, Improved photon upconversion photoluminescence and intrinsic optical bistability from a rare earth co-doped lanthanum oxide phosphor via Bi^{3+} doping, *New J. Chem.*, 2018, **42**, 7272–7282, DOI: 10.1039/C8NJ01091A.
17 J. Xue, Z. Yu, H. M. Noh, B. R. Lee, B. C. Choi, S. H. Park, J. H. Jeong, P. Du and M. Song, Designing multi-mode optical thermometers via the thermochromic LaNbO4: Bi^{3+}/Ln^{3+} (Ln= Eu, Tb, Dy, Sm) phosphors, *Chem. Eng. J.*, 2021, **415**, 128977.
18 P. Du, J. Tang, W. Li and L. Luo, Exploiting the diverse photoluminescence behaviors of NaLuF4:*x*Eu^{3+} nanoparticles and g-C3N4 to realize versatile applications in white light-emitting diode and optical thermometer, *Chem. Eng. J.*, 2021, **406**, 127165, DOI: 10.1016/j.cej.2020.127165.
19 H. Lu, Y. Gao, H. Hao, G. Shi, D. Li, Y. Song, Y. Wang and X. Zhang, Judd-Ofelt analysis and temperature dependent upconversion luminescence of Er^{3+}/Yb^{3+} codoped $Gd_2(MoO_4)_3$ phosphor, *J. Lumin.*, 2017, **186**, 34–39.
20 K. Li and D. Zhu, Ratiometric optical temperature sensing properties based on up-conversion luminescence of novel NaLaTi2O6:Yb^{3+},Er^{3+}/Ho^{3+} phosphors, *Mater. Res. Bull.*, 2025, **181**, 113117, DOI: 10.1016/j.materresbull.2024.113117.
21 V. M. Goldschmidt and D. Holmsen, Geochemische verteilungsgesetze der elemente, *In Kommission bei J. Dybwad*, 1927.
22 X. Li, P. Li, Z. Wang, S. Liu, Q. Bao, X. Meng, K. Qiu, Y. Li, Z. Li and Z. Yang, Color-Tunable Luminescence Properties of Bi^{3+} in $Ca_5(BO_3)_3$ F via Changing Site Occupation and Energy Transfer, *Chem. Mater.*, 2017, **29**, 8792–8803, DOI: 10.1021/acs.chemmater.7b03151.
23 H. Li, R. Zhao, Y. Jia, W. Sun, J. Fu, L. Jiang, S. Zhang, R. Pang and C. Li, $Sr_{1.7}Zn_{0.3}CeO_4$:Eu^{3+} Novel Red-Emitting Phosphors: Synthesis and Photoluminescence Properties, *ACS Appl. Mater. Interfaces*, 2014, **6**, 3163–3169, DOI: 10.1021/am4041493.
24 P. Du, Y. Hou, W. Li and L. Luo, Ultra-high sensitivity of multicolor Sm^{3+} -doped $LiSrVO_4$ phosphors for contactless optical thermometers, *Dalton Trans.*, 2020, **49**, 10224–10231.
25 F. Ayachi, K. Saidi, K. Soler-Carracedo, M. Dammak and I. R. Martín, Coupled and non-coupled high sensitivity multi-mode ratiometric thermometry of $Ho^{3+}/Er^{3+}/Yb^{3+}$ tri-doped $YP_{0.5}V_{0.5}O_4$ phosphors, *J. Alloys Compd.*, 2023, **961**, 171146, DOI: 10.1016/j.jallcom.2023.171146.
26 F. Ayachi, K. Saidi, W. Chaabani and M. Dammak, Synthesis and luminescence properties of Er^{3+} doped and Er^{3+}–Yb^{3+} codoped phosphovanadate $YP_{0.5}V_{0.5}O_4$ phosphors, *J. Lumin.*, 2021, **240**, 118451, DOI: 10.1016/j.jlumin.2021.118451.
27 Y. Luo, J. Wen, J. Zhang, J. Canning and G.-D. Peng, Bismuth and erbium codoped optical fiber with ultrabroadband luminescence across O-, E-, S-, C-, and L-bands, *Opt. Lett.*, 2012, **37**, 3447–3449.
28 F. Ayachi, K. Saidi, M. Dammak, W. Chaabani, I. Mediavilla-Martínez and J. Jiménez, Dual-mode luminescence of Er^{3+}/Yb^{3+} codoped $LnP_{0.5}V_{0.5}O_4$ (Ln= Y, Gd, La) for highly sensitive optical nanothermometry, *Mater. Today Chem.*, 2023, **27**, 101352.
29 F. Ayachi, K. Saidi, W. Chaabani and M. Dammak, Synthesis and luminescence properties of Er^{3+} doped and Er^{3+}–Yb^{3+} codoped phosphovanadate $YP_{0.5}V_{0.5}O_4$ phosphors, *J. Lumin.*, 2021, **240**, 118451, DOI: 10.1016/j.jlumin.2021.118451.
30 A. K. Singh, Ho^{3+}:TeO_2 glass, a probe for temperature measurements, *Sens. Actuators Phys.*, 2007, **136**, 173–177, DOI: 10.1016/j.sna.2006.10.045.
31 L. Yu, H. Song, S. Lu, Z. Liu, L. Yang and X. Kong, Luminescent Properties of $LaPO_4$:Eu Nanoparticles and Nanowires, *J. Phys. Chem. B*, 2004, **108**, 16697–16702, DOI: 10.1021/jp047688c.
32 R. S. Yadav, D. Kumar, A. K. Singh, E. Rai and S. B. Rai, Effect of Bi^{3+} ion on upconversion-based induced optical heating and temperature sensing characteristics in the Er $^{3+}$/Yb^{3+} co-doped La_2O_3 nano-phosphor, *RSC Adv.*, 2018, **8**, 34699–34711, DOI: 10.1039/C8RA07438K.

33 F. Ayachi, K. Saidi and M. Dammak, Exploring luminescence quenching mechanisms and temperature sensing capabilities of $LiSrYW_3O_{12}$: Sm^{3+} phosphors, *Mater. Adv.*, 2024, **5**, 6162–6169.

34 K. Saidi, C. Hernández-Álvarez, M. Runowski, M. Dammak and I. R. Martín, Ultralow pressure sensing and luminescence thermometry based on the emissions of Er $^{3+}$/Yb^{3+} codoped $Y_2Mo_4O_{15}$ phosphors, *Dalton Trans.*, 2023, **52**, 14904–14916.

35 F. Ayachi, K. Saidi, M. Dammak, I. Mediavilla and J. Jiménez, Unlocking advanced thermometric capabilities: $BiVO_4$: Er^{3+}/Yb^{3+} nanophosphors with dual-mode up-conversion and down-shifting features, *RSC Adv.*, 2025, **15**, 655–664, DOI: 10.1039/D4RA08590F.

36 N. B. Amar, K. Saidi, C. Hernández-Álvarez, M. Dammak and I. R. Martin, Ultra-high-sensitive temperature sensing based on emission Pr^{3+} and Yb^{3+} codoped $Y_2Mo_3O_{12}$ nanostructures, *Mater. Adv*, 2025, **6**, 827–838, DOI: 10.1039/D4MA00746H.

37 F. Ayachi, K. Saidi, M. Dammak, J. J. Carvajal and M. C. Pujol, Enhancing thermometric efficiency: a wavelength excitation analysis in $LiSrGdW_3O_{12}$:Tb^{3+} for superior single band ratiometric (SBR) thermometry, *RSC Adv.*, 2024, **14**, 13494–13504, DOI: 10.1039/D4RA00626G.

38 A. Ćirić, K. Shah, M. Sekulić, B. S. Chakrabarty and M. D. Dramićanin, La_2O_2S: Er^{3+}/Yb^{3+} nanoparticles synthesized by the optimized furnace combustion technique and their high-resolution temperature sensing, *Optik*, 2021, **245**, 167690.

39 M. Fhoula, K. Saidi, C. Hernández-Álvarez, K. Soler-Carracedo, M. Dammak and I. R. Martín, Unlocking the luminescent potential of Pr^{3+}/Yb^{3+} Co-doped $Y2Mo_4O_{15}$ for advanced thermometry applications, *J. Alloys Compd.*, 2024, **979**, 173537, DOI: 10.1016/j.jallcom.2024.173537.

40 K. Saidi, I. Kachou, K. Soler-Carracedo, M. Dammak and I. R. Martín, $Ba_2YV_3O_{11}$ Er^{3+}/Yb^{3+} Nanostructures for Temperature Sensing in the Presence of Bismuth Ions, *ACS Appl. Nano Mater.*, 2023, **6**, 17681–17690, DOI: 10.1021/acsanm.3c02911.

41 Z. E. A. A. Taleb, K. Saidi and M. Dammak, Dual-mode optical ratiometric thermometry using Pr^{3+} -doped $NaSrGd(MoO_4)_3$ phosphors with tunable sensitivity, *Dalton Trans.*, 2023, **52**, 18069–18081, DOI: 10.1039/D3DT03242F.

42 Z. Wang, M. Jia, M. Zhang, X. Jin, H. Xu and Z. Fu, Trimodal Ratiometric Luminescent Thermometer Covering Three Near-Infrared Transparency Windows, *Inorg. Chem.*, 2021, **60**, 14944–14951, DOI: 10.1021/acs.inorgchem.1c02311.

43 L. Lei, X. Dai, Y. Cheng, Y. Wang, Z. Xiao and S. Xu, Dual-mode color tuning based on upconversion core/triple-shell nanostructure, *J. Mater. Chem. C*, 2019, **7**, 3342–3350, DOI: 10.1039/C8TC05467C.

44 F. Ayachi, K. Saidi, M. Dammak, W. Chaabani, I. Mediavilla-Martínez and J. Jiménez, Dual-mode luminescence of Er^{3+}/Yb^{3+} codoped $LnP_{0.5}V_{0.5}O_4$ (Ln = Y, Gd, La) for highly sensitive optical nanothermometry, *Mater. Today Chem.*, 2023, **27**, 101352, DOI: 10.1016/j.mtchem.2022.101352.

45 K. Pavani, J. P. C. do Nascimento, S. K. Jakka, F. F. do Carmo, A. J. M. Sales, M. J. Soares, M. P. F. Graça, F. J. A. de Aquino, D. X. Gouveia and A. S. B. Sombra, Analogy of different optical temperature sensing techniques in $LaNbO_4$:Er^{3+}/Yb^{3+} phosphor, *J. Lumin.*, 2021, **235**, 117992, DOI: 10.1016/j.jlumin.2021.117992.

46 L. Li, C. Guo, S. Jiang, D. K. Agrawal and T. Li, Green up-conversion luminescence of Yb^{3+} -Er^{3+} co-doped $CaLa_2ZnO_5$ for optically temperature sensing, *RSC Adv.*, 2014, **4**, 6391, DOI: 10.1039/c3ra47264g.

47 D. Manzani, J. F. da, S. Petruci, K. Nigoghossian, A. A. Cardoso and S. J. L. Ribeiro, A portable luminescent thermometer based on green up-conversion emission of Er^{3+}/Yb^{3+} co-doped tellurite glass, *Sci. Rep.*, 2017, **7**, 41596, DOI: 10.1038/srep41596.

48 J. Zhang, Y. Zhang and X. Jiang, Investigations on upconversion luminescence of $K_3Y(PO_4)_2$:Yb^{3+}-Er^{3+}/Ho^{3+}/Tm^{3+} phosphors for optical temperature sensing, *J. Alloys Compd.*, 2018, **748**, 438–445, DOI: 10.1016/j.jallcom.2018.03.127.